


Cite this: *RSC Adv.*, 2021, **11**, 39484

# Enhanced storage behavior of quasi-solid-state aluminum–selenium battery

Haiping Lei, <sup>\*ab</sup> Suqin Li<sup>b</sup> and Jiguo Tu<sup>a</sup>

The current aluminum batteries with selenium positive electrodes have been suffering from dramatic capacity loss owing to the dissolution of  $\text{Se}_2\text{Cl}_2$  products on the Se positive electrodes in the ionic liquid electrolyte. For addressing this critical issue and achieving better electrochemical performances of rechargeable aluminum–selenium batteries, here a gel-polymer electrolyte which has a stable and strongly integrated electrode/electrolyte interface was adopted. Quite intriguingly, such a gel-polymer electrolyte enables the solid-state aluminum–selenium battery to present a lower self-discharge and obvious discharging platforms. Meanwhile, the discharge capacity of the aluminum–selenium battery with a gel-polymer electrolyte is initially  $386 \text{ mA h g}^{-1}$  ( $267 \text{ mA h g}^{-1}$  in ionic liquid electrolyte), which attenuates to  $79 \text{ mA h g}^{-1}$  ( $32 \text{ mA h g}^{-1}$  in ionic liquid electrolyte) after 100 cycles at a current density of  $200 \text{ mA g}^{-1}$ . The results suggest that the employment of a gel-polymer electrolyte can provide an effective route to improve the performance of aluminum–selenium batteries in the first few cycles.

Received 3rd November 2021  
Accepted 3rd December 2021

DOI: 10.1039/d1ra08067a

rsc.li/rsc-advances

## 1. Introduction

Due to its abundant natural resources, high theoretical capacity ( $2980 \text{ mA h g}^{-1}$ )/volumetric energy density ( $8046 \text{ mA h cm}^{-3}$ ), high safety and nontoxicity, aluminum has been used as a negative material in rechargeable aluminum-ion battery (AIB) which is regarded as a potential candidate for alleviating partial resource shortages in lithium-ion batteries.<sup>1–4</sup> Up to date, one of the most essential challenges in AIB is the lack of appropriate high energy density positive electrode materials.<sup>5,6</sup> Among the potential candidates, although selenium has a lower theoretical gravimetric capacity ( $1357 \text{ mA h g}^{-1}$ ) comparing with the congener of sulfur ( $1675 \text{ mA h g}^{-1}$ ), it has similar chemical properties but higher electronic conductivity and theoretical volumetric capacity density.<sup>7–11</sup> However, as reported in the previous work, the formed  $\text{Se}_2\text{Cl}_2$  intermediate product during charging/discharging processes in aluminum–selenium (Al–Se) battery is highly soluble in ionic liquid electrolyte (ILE) and easily shuttles to the aluminum (Al) negative electrode, which will lead to the loss of the active materials, collapse of electrode interfacial and serious attenuation of Al–Se battery's capacity.<sup>7–13</sup>

Solid-state electrolytes have been studied extensively in lithium-ion batteries and sodium-ion batteries with high safety, high energy density, and low self-discharge, which can provide a promising choice to the next generation of efficient storage devices.<sup>14–17</sup> Meanwhile, the solid-state electrolyte doesn't have

good fluidity, which may play a role in relieving the dissolution of intermediate products. Furthermore, solid-state electrolyte can act as a conducting ion and a separator, which can simplify the assembly of battery and reduce the cost. As a rational substitute for the conventional ILE, the use of solid-state electrolytes has been recognized as one of the most promising routes to addressing the solubility issue of  $\text{Se}_2\text{Cl}_2$  in Al–Se batteries. Solid-state electrolytes can be divided into three main categories: gel-polymer solid electrolytes, composite polymer electrolytes and inorganic solid electrolytes.<sup>18</sup> The gel-polymer electrolyte (GPE) presents a stable and safe electrode/electrolyte interface, which can enhance the cycling stability and rate performance of the battery.<sup>19–21</sup>

From the perspective of controlling the dissolution and migration of intermediate product  $\text{Se}_2\text{Cl}_2$  in ILE, the GPE with stable and strongly integrated electrode/electrolyte interface was employed in this work to study the effects on the dynamics, specific capacity, and cycling stability of Al–Se battery. After using GPE, Al–Se battery presents a lower self-discharge and obvious discharging platforms. Meanwhile, the first discharge capacity of Al–Se battery increases to  $386 \text{ mA h g}^{-1}$  at the current density of  $200 \text{ mA g}^{-1}$ . The GPE can effectively inhibit the  $\text{Se}_2\text{Cl}_2$  diffusion and retain a strongly integrated electrolyte/electrode structure. These remarkable performances can be ascribed to the immobilization of  $\text{Se}_2\text{Cl}_2$  imparted by GPE and the construction of a robust integrated GPE/electrode interface.

## 2. Experimental section

### Materials

Al foil (99.99%) was purchased from Research Institute for Nonferrous Metals (Beijing, P. R. China). Tantalum foil (Ta,

<sup>a</sup>State Key Laboratory of Advanced Metallurgy, University of Science and Technology Beijing, Beijing 100083, PR China. E-mail: leihaiping0214@ustb.edu.cn

<sup>b</sup>School of Metallurgical and Ecological Engineering, University of Science and Technology Beijing, Beijing 100083, PR China



99.9%) and molybdenum foil (Mo, 99.0%) were obtained from Sheng Yuan Metal Co. Ltd.  $\text{SeO}_2$  (99%, Aladdin), poly-cyclodextrin (98.0%, Aladdin), ascorbic acid (99.5%, Aladdin), acrylamide (98.5%, Alfa Aesar), dichloromethane (DCM,  $\geq 99\%$ , Alfa Aesar), 1-ethyl-3-methylimidazolium chloride ([EMIm]Cl, 97%, Acros Chemicals), polyvinylidene difluoride binder (PVDF, Macklin), *N*-methyl-2-pyrrolidinone (NMP,  $\geq 99.0\%$ , Acros Chemicals), anhydrous aluminum chloride ( $\text{AlCl}_3$ , 99.999%, Sigma Aldrich), and 2,2'-azodiisobutyronitrile (AIBN,  $>98\%$ , TCI) were purchased from commercial sources.

## Materials preparation

**Preparation of selenium nanowires.** The preparation schematic diagram of selenium nanowires is shown in Fig. 1(a), which is the synthesis method in the ref. 22 and 23. The specific process is as follows:  $\text{SeO}_2$  (0.5 g) and poly-cyclodextrin (0.5 g) were added in distilled water (100 mL), and stirred magnetically until the particles were completely dissolved. Ascorbic acid

(0.53 g) was added into 100 mL of distilled water and stirred magnetically until the particles completely dissolved. Then the solution was mixed together and stirred for 4 hours constantly. The products were centrifugally washed with alcohol and deionized water for 3 times, and then the products were re-dispersed in the alcohol, and finally dried in a  $60^\circ\text{C}$  oven.

Al foil (thickness of  $50\ \mu\text{m}$ ), Ta foil (thickness of  $10\ \mu\text{m}$ ) and Mo foil (thickness of  $20\ \mu\text{m}$ ) were prepared and cleaned in ethanol by ultrasound (KQ2200E, 40 kHz). The positive electrodes were prepared by 60 wt% of treated selenium nanowire, 30 wt% of acetylene black, and 10 wt% of PVDF in NMP, and casted onto a Ta foil current collector after fully stirring. Then Mo foil was attached to Ta foil by conducting tape after drying.

## Assembling the soft-package Al-Se battery with ILE (Se/ILE/Al battery)

Room temperature ILE was made by mixing [EMIm]Cl and  $\text{AlCl}_3$  in an argon-atmosphere glove box ( $[\text{O}_2] < 0.1\ \text{ppm}$ ,  $[\text{H}_2\text{O}] < 0.1$

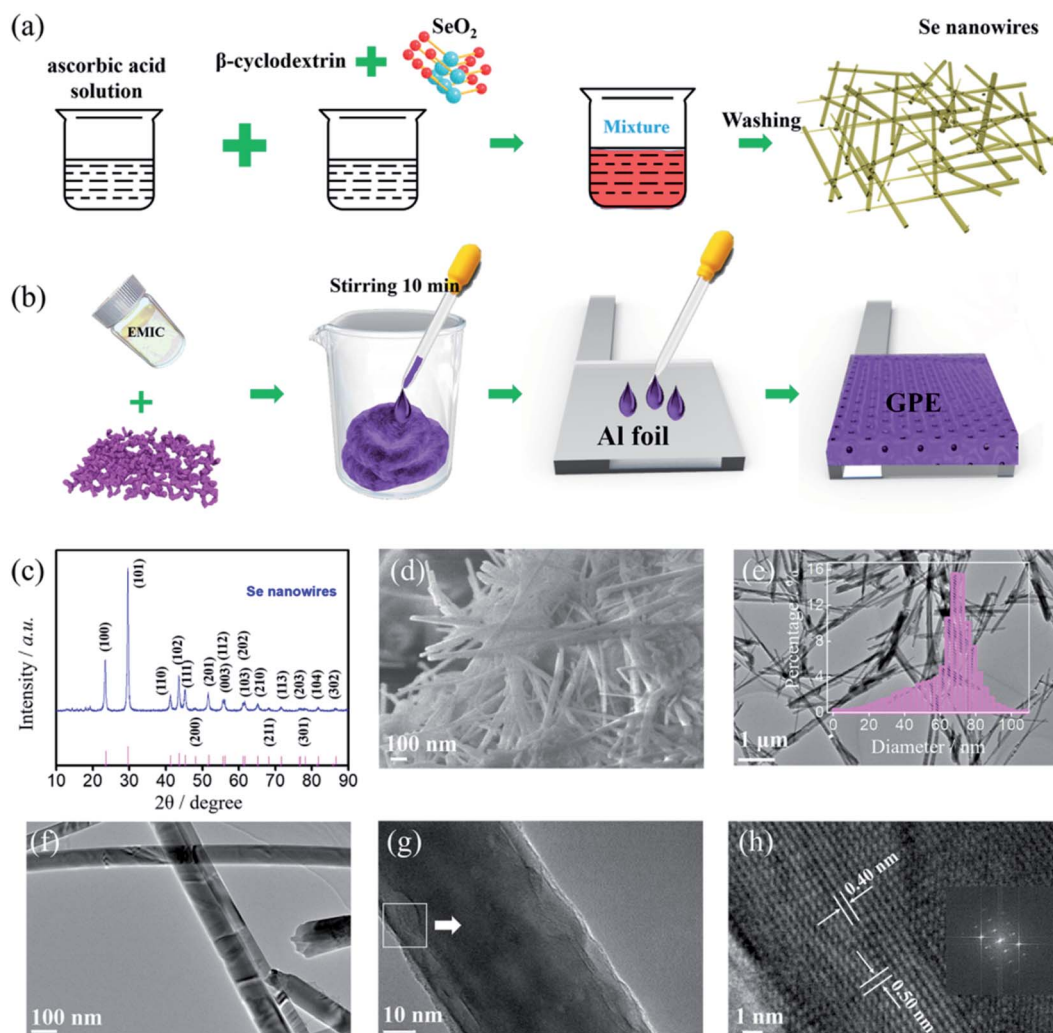


**Fig. 1** (a) Schematic diagram of the preparation of selenium nanowires. (b) Schematic diagram of the preparation of the GPE. (c) XRD pattern of as-prepared selenium nanowires. (d) FESEM images of selenium nanowires. (e and f) TEM images of selenium nanowires. Inset: the histogram of Se nanowires diameter. (g and h) HRTEM images of selenium nanowires.

ppm), and  $\text{AlCl}_3$  was slowly dissolved in  $[\text{EMIm}]\text{Cl}$  with the molar ratio 1.3 : 1. The resulting light-yellow and transparent liquid was stirred at room temperature for 30 min. And then the  $([\text{EMIm}]\text{Al}_x\text{Cl}_y)$  ionic liquid electrolytes were standing at least 12 h before used. Positive electrode, Al foil negative electrode, glass fiber (GF/A, Whatman) separator, and Al-plastic film were assembled, injected electrolyte and sealed in an Ar-filled glove box.

### Assembling the soft-package Al-Se battery with GPE (Se/GPE/Al battery)

GPE was prepared by *in situ* gelation method in an argon-atmosphere glove box as shown in Fig. 1(b).<sup>20</sup> First,  $\text{AlCl}_3$  (1.34 g) and acrylamide (0.7 g) were slowly dissolved in methylene chloride (12 g) under vigorous stirring until the solution turned light yellow to achieve complexation of acrylamide and  $\text{AlCl}_3$ . Then, as-prepared 1.5 mol ratio of  $[\text{EMIm}]\text{Al}_x\text{Cl}_y$  electrolyte (8 g) was added into the solution. Subsequently, the polymerization process started after adding the initiator AIBN (0.007 g). Finally, the solution was casting onto Al foil until the mixing appeared partially solidified state and the sample was placed in the glove box for 12 h to get the GPE membrane. The quasi-solid-state Al-Se battery were fabricated with the coated positive electrode and the GPE membrane formed on the Al foil negative electrode, followed by assembling them into a Al-plastic film and sealing with a heat sealing machine (BLEUETS FR-300B, sealing temperature below 300 °C) in an Ar-filled glove box.

### Electrochemical tests

CV measurements were performed at scan rates of 1, 5, 10  $\text{mV s}^{-1}$  over voltage range of 0.01 to 2.3 V *versus*  $\text{Al}/\text{Al}^{3+}$  by a CHI 660E (Shanghai, China) electrochemical workstation in two-electrode mode. Galvanostatic charge/discharge tests were carried out at current densities of 200, 400, 600  $\text{mA g}^{-1}$  with the potential window of 0.01 to 2.2 V at room temperature using Neware BTS-53 tester. Electrochemical impedance spectroscopy measurements (CHI 660E) were conducted at fresh, charged and discharge cycled cells in the frequency range from 100 kHz to 0.01 Hz. Self-discharge (Neware BTS-53) was performed by resting for 6 h and different voltage.

### Characterization

Field emission scanning electron microscopy (FESEM) were taken to determine the morphology and composition contents of the original materials and cycled materials on a JEOL JSM-6701F. High-resolution transmission electron microscopy (HRTEM) analyses were conducted on a JEOL JEM-2010. The phase structures of the original materials were obtained from X-ray diffraction (XRD, Rigaku, D/max-RB) with a Cu K $\alpha$  wave.

## 3. Results and discussion

The synthesis procedure of selenium nanowires is schematically shown in Fig. 1(a). Under the facile two-step operation, the as-prepared selenium nanowires were obtained. In order to characterize the crystallinity and phase of as prepared selenium

nanowires, the synthesized materials were tested by XRD. From Fig. 1(c), all the reflections could be assigned to a pure hexagonal phase of selenium (JCPDS card no. 06-0362) with lattice parameters of  $a = 4.3662 \text{ \AA}$  and  $c = 4.9536 \text{ \AA}$ .<sup>22–26</sup> No residual phase is detected, indicating that the successful preparation of selenium products with high crystallinity and purity.

Fig. 1(d–h) shows the morphology of as-prepared selenium samples by FESEM and TEM. The FESEM image (Fig. 1(d)) reveals the obtained products have the wire structure and are in large scale with uniform size and smooth shape, which are typical one-dimensional wire materials. Meanwhile, as can be seen from the TEM images amplified in Fig. 1(e) and (f), the nanowires have relatively uniform diameter and smooth surfaces. The diameter distribution of Se nanowires is presented in Fig. 1(e), suggests the uniform diameter size is about 70 nm. The HRTEM image in Fig. 1(h) shows the lattice fringes of Se nanowire are arranged in parallel. Meanwhile, the clear lattice fringes with  $d$ -spacing of  $\sim 0.4 \text{ nm}$  and  $0.5 \text{ nm}$  correspond to the (100) and (001) lattice planes of hexagonal phase Se, revealing that the nanowire was single crystalline.<sup>27–29</sup> The inset describes a fast Fourier transform (FFT) of the image of Fig. 1(h) which is equivalent to an electron diffraction pattern. The HRTEM image and FFT pattern demonstrate that the nanowire has a preferential orientation along the (001) direction.<sup>29</sup>

The Al-Se battery was fabricated with synthesized well-defined nanostructure selenium nanowires as the positive electrode, Al foil as the negative electrode, and GPE or ILE as the electrolyte. Obviously, the selenium nanowires have been agglomerated by the PVDF binder and the morphology of selenium nanowires on the positive electrode before cycling can be clearly observed in Fig. 2(a). GPE has certain mechanical strength, can be used as a block between the positive electrode and negative electrode which means the battery with GPE doesn't need GF/A separator. The open circuit potential of the untested battery was detected and it was found that the open circuit potentials of the GPE and ILE battery were both about 1.5 V as shown in Fig. 2(b) and (c).

The typical CV measurements of Al-Se batteries with ILE and GPE in the voltage range of 0.01–2.3 V were carried out at a scan rate of 1  $\text{mV s}^{-1}$ , as shown in Fig. 2(b) and (c). The CV curves of Se/ILE/Al battery displays the obvious reduction peaks ( $\sim 1.52$  and  $1.65 \text{ V}$ ) and the corresponding oxidation peaks ( $\sim 1.53$  and  $1.85 \text{ V}$ ). The charging and discharge platforms of Al-Se battery are higher than Al-S battery's (charging platform of  $\sim 1.25 \text{ V}$ , and discharge platform of  $\sim 0.75 \text{ V}$ ),<sup>30–32</sup> Al-CuO battery's (charging platform of  $\sim 0.8 \text{ V}$ , and discharge platform of  $\sim 0.6 \text{ V}$ ),<sup>33</sup> and Al-CuS@C battery (charging platform of  $\sim 1.5 \text{ V}$ , and discharge platform of  $\sim 1.0$  and  $0.4 \text{ V}$ ).<sup>34</sup> Meanwhile, they are similar with the Al-Te battery's (charging platform of  $\sim 1.6$  and  $1.8 \text{ V}$ , discharge platform of  $\sim 1.5$  and  $0.45 \text{ V}$ ).<sup>35,36</sup> Therefore, Se as the positive electrode material of AIB is competitive, even though the non-overlapping CV curves with cycling may be caused by the loss of reactants dissolved in the ILE. For the Se/GPE/Al battery, the reduction peaks shift to 1.73 and 1.47 V, the oxidation peaks shift to higher potentials (1.59 and 1.91 V). In addition, the peak current densities of the Se/GPE/Al battery are





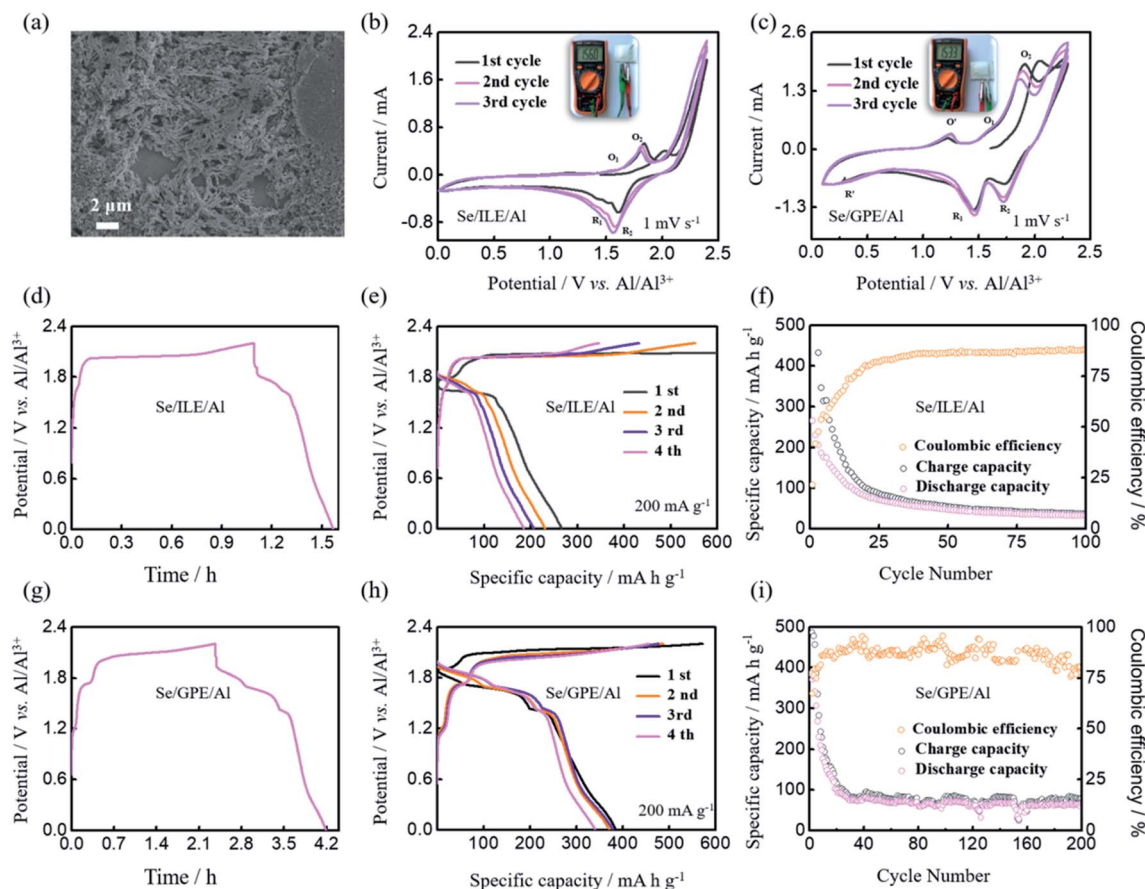


Fig. 2 (a) FESEM image of positive electrode before cycling. (b and c) The initial three CV curves at a scan rate of  $1 \text{ mV s}^{-1}$  of Al–Se batteries with ILE and GPE. (d and g) The charge/discharge profiles of Al–Se batteries with ILE and GPE. (e and h) The charge/discharge curves at  $200 \text{ mA g}^{-1}$  of Al–Se batteries with ILE and GPE. (f and i) The corresponding cycling performance and coulombic efficiency with ILE and GPE.

obviously higher than those of Se/ILE/Al battery. What's more, almost overlapped CV curves are observed from the second cycle, indicating the good reversibility of Se electrode in Se/GPE/Al battery. An additional pair of oxidation–reduction peaks were appeared with the reduction peak at  $0.32 \text{ V}$  and the oxidation peak at  $1.24 \text{ V}$ , probably caused by the side reaction of GPE.

Meanwhile, further galvanostatic charge and discharge tests were implemented at the current density of  $200 \text{ mA g}^{-1}$  to assess the energy storage capacity of the Al–Se batteries with ILE and GPE, as shown in Fig. 2(d–i). The typical charge/discharge curves are shown in Fig. 2(d) and (g), which shows the obvious charging platforms ( $\sim 1.67$  and  $2.0 \text{ V}$  of Se/ILE/Al battery,  $\sim 1.21$ ,  $1.69$  and  $2.0 \text{ V}$  of Se/GPE/Al battery) and discharge platforms ( $\sim 1.60$  and  $1.78 \text{ V}$  of Se/ILE/Al battery,  $\sim 1.85$ ,  $1.65$  and  $1.39 \text{ V}$  of Se/GPE/Al battery). Se/GPE/Al battery exhibits one more pair and more obvious charging and discharging platforms than Se/ILE/Al battery. It is clear that the Se/GPE/Al battery exhibits nearly the same initial specific charge capacity ( $571 \text{ mA h g}^{-1}$ ) comparing with the Se/ILE/Al battery's ( $594 \text{ mA h g}^{-1}$ ) at the current density of  $200 \text{ mA g}^{-1}$  (Fig. 2(e) and (h)). The 1<sup>st</sup>, 2<sup>nd</sup>, 3<sup>rd</sup>, and 4<sup>th</sup> discharge capacities of the Se/GPE/Al battery at  $200 \text{ mA g}^{-1}$  are  $386$ ,  $371$ ,  $378$ , and  $340 \text{ mA h g}^{-1}$ , respectively, while the corresponding capacities of the Se/ILE/Al battery are only  $267$ ,  $232$ ,  $206$ , and  $184 \text{ mA h g}^{-1}$ ,

respectively. The charge/discharge behaviors are in good agreement with the CV measurements in Fig. 2(c). Se/ILE/Al battery exhibits a discharge capacity of  $32 \text{ mA h g}^{-1}$  over 100 cycles (Fig. 2(f)). In contrast, Se/GPE/Al battery delivers a higher discharge capacity of  $79 \text{ mA h g}^{-1}$  over 100 cycles (Fig. 2(i)) comparing with Se/ILE/Al battery. Interestingly, the Se/GPE/Al battery shows a much higher rate performance and better reversibility than the Se/ILE/Al battery. To understand the kinetics of the Al–Se batteries with different electrolyte deeply, CV curves were further investigated at the scan rates of  $1$ ,  $5$  and  $10 \text{ mV s}^{-1}$  (Fig. 3(a) and (b)). It is found that the peak current intensities of redox peaks are gradually enhanced with the increase of scanning rate. The oxidation peak voltage is offset to the positive direction, and the reduction peak voltage is offset to the negative direction, further indicating the existence of electrode polarization phenomenon of Al–Se battery. The charge/discharge profiles of Se/ILE/Al and Se/GPE/Al battery at different current densities are presented in Fig. 3(c) and (d). The specific discharge capacities of the Se/GPE/Al battery at the current densities of  $400$ ,  $600 \text{ mA g}^{-1}$  are  $233$ ,  $159 \text{ mA h g}^{-1}$ , respectively, while the corresponding capacities of Se/ILE/Al battery are only  $135$ ,  $72 \text{ mA h g}^{-1}$ , reflecting that the Se/GPE/Al battery is robust and highly stable.



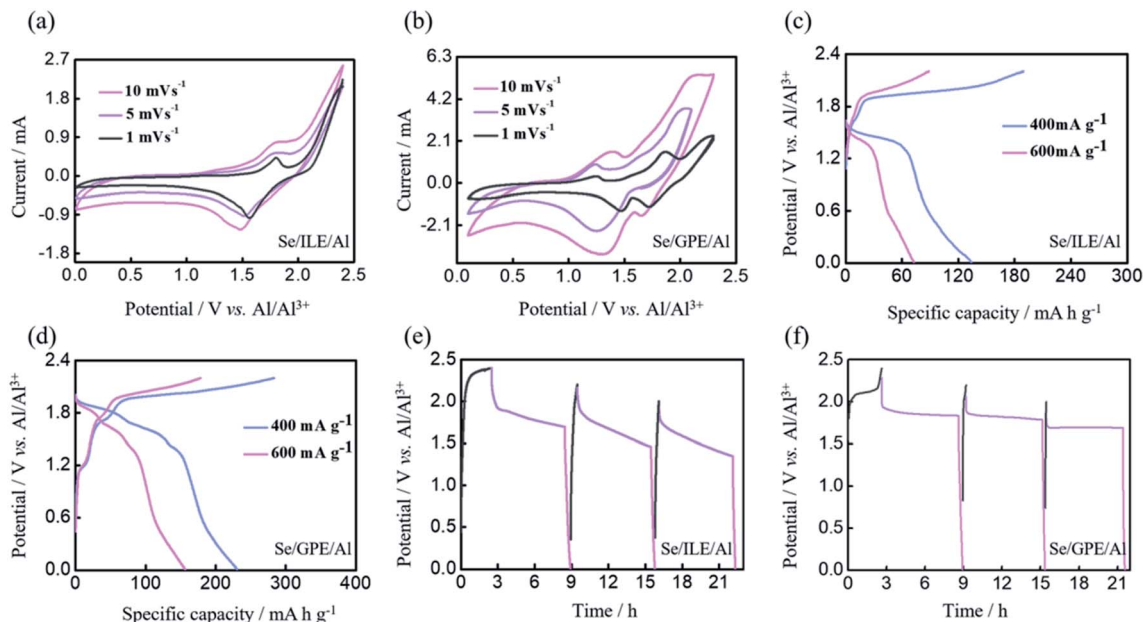


Fig. 3 (a and b) The CV curves at scan rates of 1, 5, 10  $\text{mV s}^{-1}$  of Al–Se batteries with ILE and GPE. (c and d) The charge/discharge curves at 400 and 600  $\text{mA g}^{-1}$  of Al–Se batteries with ILE and GPE. (e and f) The self-discharge behaviors of Al–Se batteries with ILE and GPE under different charge potentials.

Fig. 3(e) and (f) shows the self-discharge behaviors of Al–Se battery with ILE and GPE which the batteries were rested for 6 h after charging to 2.0, 2.2, and 2.4 V. The noticeable voltage variation at different charging voltages indicates that the higher charging voltage of Al–Se battery is, the more obvious voltage drop will be. Meanwhile, the voltage of Se/GPE/Al battery firstly falls fast, and then remains at about 1.83, 1.76, and 1.67 V, respectively, which are much higher than the voltages of Se/ILE/Al battery (1.69, 1.50 and 1.36 V, respectively), further implying more stable Se/GPE/Al battery. However, comparing these with commercial lithium-ion batteries,<sup>37</sup> the self-discharge of Al–Se battery is still high. Self-discharge behavior may be caused by irreversible side reactions in the battery, including the reactant dissolved in electrolyte, and side reaction of impurities in electrolyte.

Electrochemical impedance spectroscopy (EIS) was investigated as shown in Fig. 4 to evaluate the interfacial resistance of Al–Se batteries using ILE and GPE electrolyte. Nyquist plots of Se/ILE/Al battery and Se/GPE/Al battery at the different charging states (pristine, fully charged, and fully discharged) are composed of a depressed semicircle corresponding to the charge transfer resistance in the high-to-medium frequency region and a sloping line relating to the ion diffusion ability within the electrodes in the low frequency region as shown in Fig. 4(a) and (c), and the corresponding enlargement curves were shown in Fig. 4(b) and (d). It is seen that the interfacial resistance ( $R_f$ ) in the Se/ILE/Al battery increases from 1.86  $\Omega$  to 3  $\Omega$  (charging) and 2.4  $\Omega$  (discharging), and the corresponding charge transfer resistance ( $R_{ct}$ ) rises from 28.8  $\Omega$  to 39.4  $\Omega$  (charging) and 32.9  $\Omega$  (discharging). The  $R_f$  in the Se/GPE/Al battery increases from 15.8  $\Omega$  to 23.1  $\Omega$  (charging) and 20.7  $\Omega$  (discharging), and the corresponding charge transfer resistance

( $R_{ct}$ ) increases from 10.5  $\Omega$  to 11.5  $\Omega$  (charging) and 23.7  $\Omega$  (discharging). The higher  $R_f$  of GPE than that of ILE may be due to its poor fluidity. The relationship between the real part of impedance ( $Z'$ ) and the angular frequency ( $\omega^{-1/2}$ , in the low frequency region) are shown in Fig. 4(e) and (f). The ion diffusion coefficient ( $D$ ) can be calculated from the formula as following:<sup>38,39</sup>

$$D = \frac{R^2 T^2}{2A^2 n^4 F^4 C^2 \sigma^2} \quad (1)$$

where  $R$  is the gas constant,  $T$  is the absolute temperature,  $A$  is the surface area of the electrode,  $n$  is the number of the electrons per molecule attending the electronic transfer reaction,  $F$  is the Faraday constant,  $C$  is the concentration, and  $\sigma$  is the slope of the line  $Z'$  versus  $\omega^{-1/2}$  (shown in Fig. 4(e) and (f)). The  $\sigma$  values of GPE (306.9 before cycling, 494.5 at the discharged state, and 368.2 at the charged state) are much lower than those of ILE (662.8 before cycling, 931.4 at the discharged state, and 886.2 at the charged state). Accordingly, the  $D$  values of GPE are much higher than those of ILE, demonstrating fast ion diffusion kinetics within the GPE system. Therefore, the electrochemical performances of Al–Se batteries have been improved based on the favorable ion diffusion kinetics by using GPE.

The morphology of the 50<sup>th</sup> cycled GPE was characterized by FESEM as shown in Fig. 5(a) and (b), exhibiting the unsmooth but coarse, irregular feature on the electrolyte surface. The GPE skeleton structure is obvious, which has a certain mechanical toughness. After cycling, a lot of gullies appear in the GPE. Inset of Fig. 5(a) is the corresponding EDS spectrum, revealing the Al, Cl and O elements existing. The O element exists in the aluminum hydroxide which was produced by the electrolyte hydrolyzing during the preparation of FESEM samples. The EDS



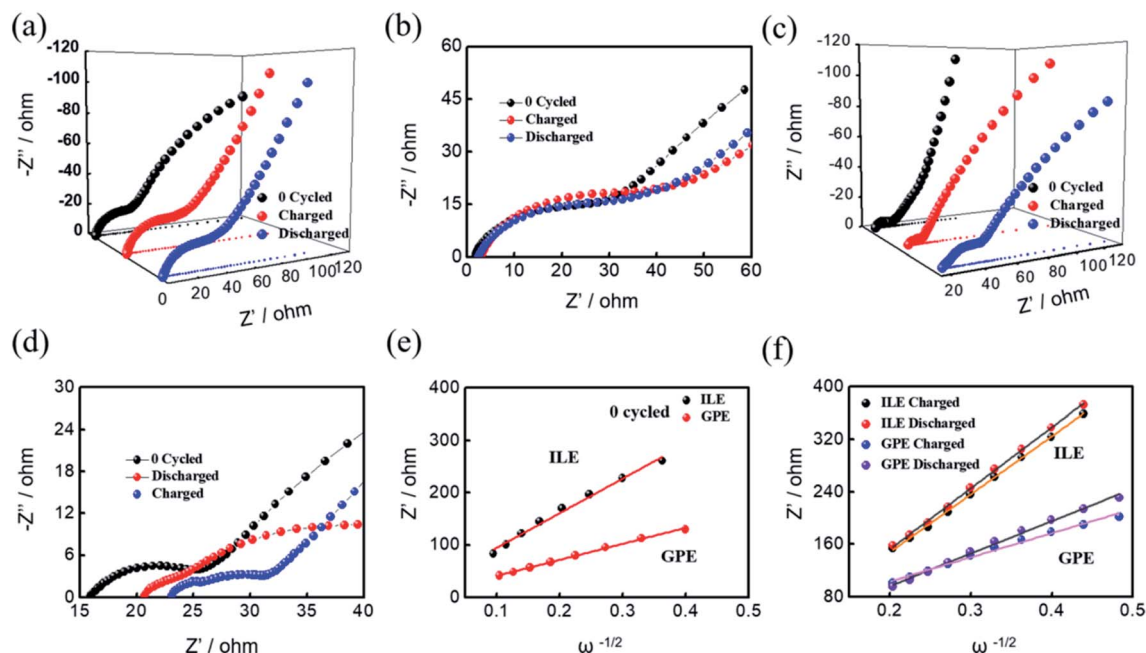


Fig. 4 (a and b) Electrochemical impedance spectroscopy of Al–Se battery with ILE at different conditions as marked. (c and d) Electrochemical impedance spectroscopy of Al–Se battery with GPE at different conditions as marked. (e) Relationships of  $Z'$  versus  $\omega^{-1/2}$  for Al–Se batteries with ILE and GPE before cycling. (f) Relationships of  $Z'$  versus  $\omega^{-1/2}$  for Al–Se batteries with ILE and GPE after cycling.

mapping of Al and Cl elements on the surface of the electrolyte are shown in Fig. 5(c) and (d), further confirming that the main ingredients are Al and Cl in the electrolyte after cycling. These results confirm the successful construction of a robust integrated GPE/selenium positive electrode interface.

The optical images of cycled Al–Se batteries with different electrolytes are shown in Fig. 6(a), which is evident that the positive materials battery has been dissolved in ILE but not obvious in GPE. Fig. 6(b) shows the FESEM image of cycled positive electrode of Al–Se battery after 50<sup>th</sup> cycled with ILE. The

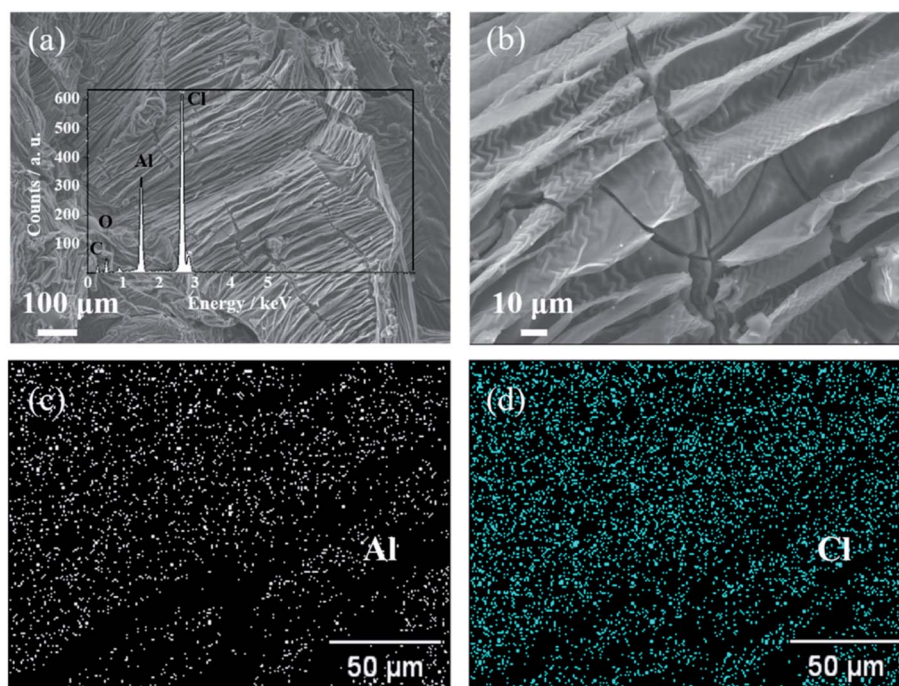


Fig. 5 (a and b) FESEM images of the 50<sup>th</sup> cycled GPE. Inset: the corresponding EDS spectrum of cycled GPE. (c and d) EDS mapping images of Al and Cl of the 50<sup>th</sup> cycled GPE.



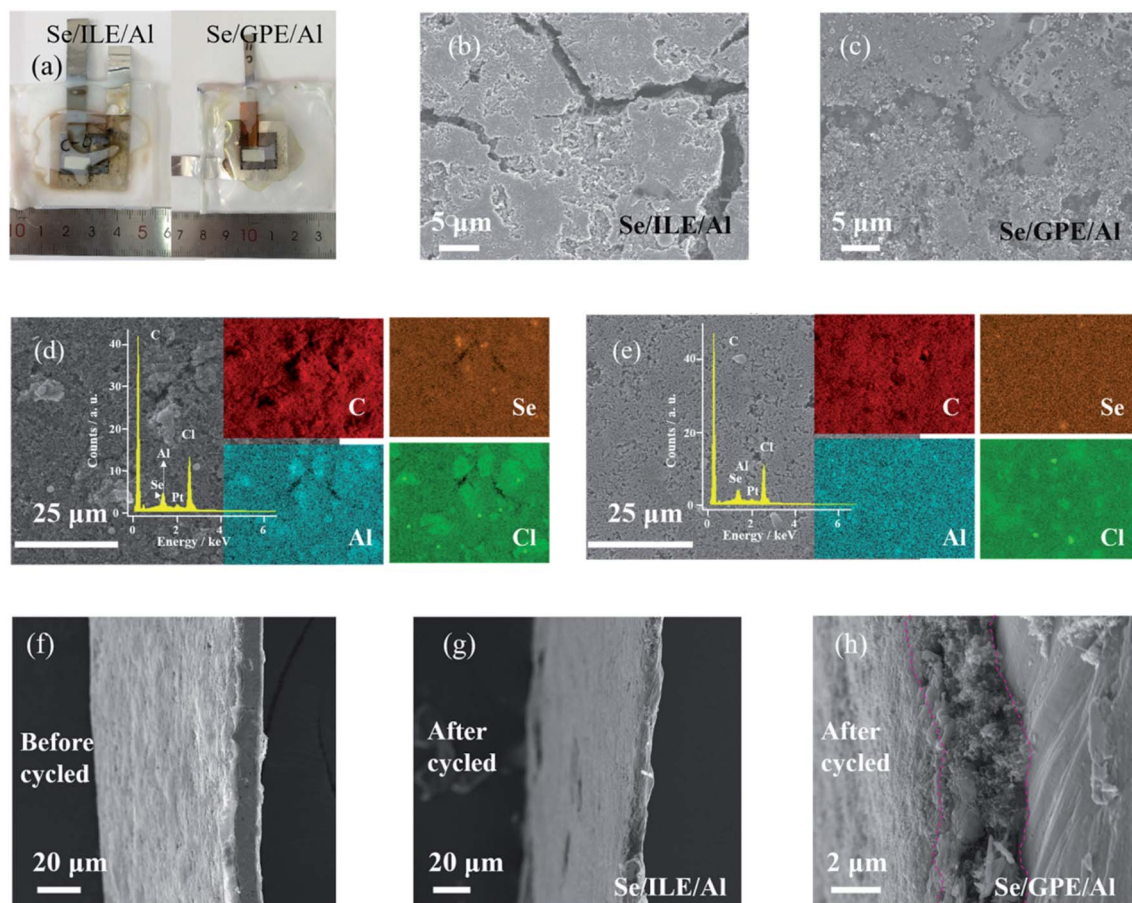


Fig. 6 (a) Optical images of cycled Al–Se batteries with ILE and GPE. (b and c) FESEM image of cycled positive electrode of Al–Se batteries with ILE and GPE. (d) FESEM and corresponding EDS mapping images of Al, Cl, C, and Se of cycled positive electrode in ILE. (e) FESEM and corresponding EDS mapping images of Al, Cl, C, and Se of cycled positive electrode in GPE. (f–h) The cross-sectional FESEM image of positive electrode before cycling, 50<sup>th</sup> cycled in ILE, and 50<sup>th</sup> cycled in GPE.

morphology of selenium nanowires is no longer visible, and obvious cracks and holes are appeared, demonstrating the dissolved behavior of selenium nanowires after cycling in ILE. Fig. 6(c) shows FESEM image of the 50<sup>th</sup> cycled positive electrode of Al–Se battery with GPE. It is also found that there are many cracks, holes and no obvious selenium nanowires. Fig. 6(d) shows the FESEM and corresponding EDS mapping images, revealing the distribution of Al, Cl, C, Pt, and Se in cycled positive electrode after 50<sup>th</sup> cycling in ILE. The obvious minor peak between Se and Cl is the element Pt which was sputtered on the surface of the samples for an additional conductive thin layer before the FESEM test. The contents of Al, Cl, C, and Se measured in EDS spectrum are approximately 0.82 wt%, 8.68 wt%, 88.33 wt%, and 2.17 wt% after removing the element Pt, respectively. The FESEM and corresponding EDS mapping images of Al, Cl, C, and Se of 50<sup>th</sup> cycled positive electrode in GPE as shown in Fig. 6(e), demonstrating no obvious difference with those in ILE. The EDS spectrum reveals the contents of Al, Cl, C, and Se are approximately 0.78 wt%, 6.43 wt%, 90.68 wt%, and 2.12 wt% after removing the element Pt, respectively. These indicate that although GPE can greatly improve the battery performance, the selenium nanowires still

cannot avoid being completely dissolved in GPE after 50<sup>th</sup> cycling process.

Fig. 6(f–h) shows the cross-sectional FESEM image of positive electrode before cycling, 50<sup>th</sup> cycled in ILE, and 50<sup>th</sup> cycled in GPE. It is obvious that the cross-section widths of selenium positive electrodes become narrower after reaction, which further confirming the dissolving effect. Meanwhile, the cross-section width of selenium positive electrode in GPE becomes smaller than ILE which probably due to the stickiness of GPE during sample preparation. As can be demonstrated from the Fig. 7, the poor fluidity, the stable and safe electrode–electrolyte interface of GPE can relieve the dissolution of the electrode materials and intermediate product to a certain extent than ILE, further greatly improving the electrochemical behaviors of the battery in the first few cycles. However, after hundreds of cycles, it still can't stop the dissolution. Further research is needed on ways to mitigate the dissolution.

## 4. Conclusions

In summary, a quasi-solid-state AIB has been established using the GPE between Se positive electrode and Al negative electrode,



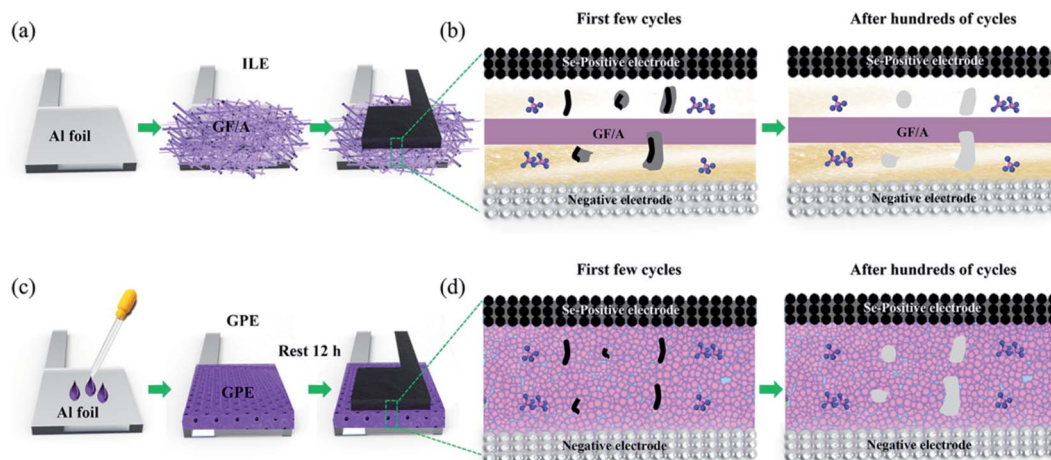


Fig. 7 (a) Assembly diagram of the preparation of ILE. (b) Schematic diagram of intermediate product diffusion into the ILE. (c) Assembly diagram of the preparation of the GPE. (d) Schematic diagram of intermediate product diffusion into the GPE.

aiming to well addressing the critical capacity attenuation problems in the Al–Se battery with liquid electrolytes. Interestingly, compared with ILE, the incorporation of GPE in Al–Se battery shows lower self-discharge and obvious discharging platforms, and also greatly enhances the rate capacity and cycle stability. The GPE successfully prevent the loss of  $\text{Se}_2\text{Cl}_2$  into the ILE, increases the utilization of the active materials, and promotes electronic conductivity and fast reaction kinetics in the first few cycles. Such performance improvement is probably attributed to the strong immobilization of soluble intermediate products by GPE.

## Conflicts of interest

The authors declare no competing financial interests.

## Acknowledgements

This work was supported by National Natural Science Foundation of China (51874019), Fundamental Research Funds for the Central Universities (FRF-TP-20-045A1), and China Postdoctoral Science Foundation (2020M680347 and 2021T140051).

## References

- 1 N. Jayaprakash, S. K. Das and L. A. Archer, *Chem. Commun.*, 2011, **47**, 12610–12612.
- 2 H. Sun, W. Wang, Z. Yu, Y. Yuan, S. Wang and S. Jiao, *Chem. Commun.*, 2015, **51**, 11892–11895.
- 3 M. C. Lin, M. Gong, B. G. Lu, Y. P. Wu, D. Y. Wang, M. Y. Guan, M. Angell, C. X. Chen, J. Yang, B. J. Hwang and H. J. Dai, *Nature*, 2015, **520**, 325–328.
- 4 J. Tu, W. L. Song, H. Lei, Z. Yu, L.-L. Chen, M. Wang and S. Jiao, *Chem. Rev.*, 2021, **121**, 4903–4961.
- 5 Y. Zhang, S. Liu, Y. Ji, J. Ma and H. Yu, *Adv. Mater.*, 2018, **30**, 1706310.
- 6 M. Jiang, C. Fu, P. Meng, J. Ren, J. Wang, J. Bu, A. Dong, J. Zhang, W. Xiao and B. Sun, *Adv. Mater.*, 2021, 2102026.
- 7 C. P. Yang, S. Xin, Y. X. Yin, H. Ye, J. Zhang and Y. G. Guo, *Angew. Chem., Int. Ed.*, 2013, **52**, 8363–8367.
- 8 X. Huang, Y. Liu, C. Liu, J. Zhang, O. Noonan and C. Yu, *Chem. Sci.*, 2018, **9**, 5178–5182.
- 9 Y. Kong, A. K. Nanjundan, Y. Liu, H. Song, X. Huang and C. Yu, *Small*, 2019, **15**, 1904310.
- 10 S. C. Wu, Y. Ai, Y. Z. Chen, K. Wang, T. Y. Yang, H. J. Liao, T. Y. Su, S. Y. Tang, C. W. Chen, D. C. Wu, Y. C. Wang, A. Manikandan, Y. C. Shih, L. Lee and Y. L. Chueh, *ACS Appl. Mater. Interfaces*, 2020, **12**, 27064–27073.
- 11 H. Lei, S. Jiao, J. Tu, W. L. Song, X. Zhang, M. Wang, S. Li, H. Chen and D. Fang, *Chem. Eng. J.*, 2020, **385**, 123452.
- 12 S. Liu, X. Zhang, S. He, Y. Tang, J. Wang, B. Wang, S. Zhao, H. Su, Y. Ren, L. Zhang, J. Huang, H. Yu and K. Amine, *Nano Energy*, 2019, **66**, 104159.
- 13 Z. Li, J. Liu, X. Huo, J. Li and F. Kang, *ACS Appl. Mater. Interfaces*, 2019, **11**, 45709–45716.
- 14 M. Liu, D. Zhou, Y.-B. He, Y. Fu, X. Qin, C. Miao, H. Du, B. Li, Q.-H. Yang, Z. Lin, T. S. Zhao and F. Kang, *Nano Energy*, 2016, **22**, 278–289.
- 15 Z. Gao, H. Sun, L. Fu, F. Ye, Y. Zhang, W. Luo and Y. Huang, *Adv. Mater.*, 2018, **30**, 1705702.
- 16 Z. Yu, S. L. Shang, D. Wang, Y. C. Li, H. P. Yennawar, G. Li, H.-T. Huang, Y. Gao, T. E. Mallouk, Z. K. Liu and D. Wang, *Energy Storage Mater.*, 2019, **17**, 70–77.
- 17 Q. Zhao, S. Stalin, C. Z. Zhao and L. A. Archer, *Nat. Rev. Mater.*, 2020, **5**, 229–252.
- 18 C. Zhao, L. Liu, X. Qi, Y. Lu, F. Wu, J. Zhao, Y. Yu, Y.-S. Hu and L. Chen, *Adv. Energy Mater.*, 2018, **8**, 1703012.
- 19 X. G. Sun, Y. Fang, X. Jiang, K. Yoshii, T. Tsuda and S. Dai, Polymer gel electrolytes for application in aluminum deposition and rechargeable aluminum ion batteries, *Chem. Commun.*, 2016, **52**, 292–295.





- 20 Z. Yu, S. Jiao, S. Li, X. Chen, W. L. Song, T. Teng, J. Tu, H.-S. Chen, G. Zhang and D. N. Fang, *Adv. Funct. Mater.*, 2018, **29**, 1806799.
- 21 Z. Yu, S. Jiao, J. Tu, W.-L. Song, H. Lei, H. Jiao, H. Chen and D. Fang, *J. Mater. Chem. A*, 2019, **7**, 20348–20356.
- 22 Q. Li and W. W. Yam, *Chem. Commun.*, 2006, **9**, 1006–1008.
- 23 J. Zhang, Y. Xu, L. Fan, Y. Zhu, J. Liang and Y. Qian, *Nano Energy*, 2015, **13**, 592–600.
- 24 L. Cheng, M. Shao, D. Chen, X. Wei, F. Wang and J. Hua, *J. Mater. Sci.: Mater. Electron.*, 2008, **19**, 1209–1213.
- 25 L. Liu, Y. Hou, X. Wu, S. Xiao, Z. Chang, Y. Yang and Y. Wu, *Chem. Commun.*, 2013, **49**, 11515–11517.
- 26 B. Gates, B. Mayers, A. Grossman and Y. Xia, *Adv. Mater.*, 2002, **14**, 1749–1752.
- 27 M. Jia, C. Mao, Y. Niu, J. Hou, S. Liu, S. Bao, J. Jiang, M. Xu and Z. Lu, *RSC Adv.*, 2015, **5**, 96146–96150.
- 28 L. B. Luo, J. S. Jie, Z. H. Chen, X. J. Zhang, X. Fan, G. D. Yuan, Z. B. He, W. F. Zhang, W. J. Zhang and S. T. Lee, *J. Nanosci. Nanotechnol.*, 2009, **9**, 6292–6298.
- 29 Q. Xie, J. Liu, J. Liang, W. Yu and Y. Qian, *J. Nanosci. Nanotechnol.*, 2006, **6**, 857–862.
- 30 T. Gao, X. Li, X. Wang, J. Hu, F. Han, X. Fan, L. Suo, A. J. Pearse, S. B. Lee, G. W. Rubloff, K. J. Gaskell, M. Noked and C. Wang, *Angew. Chem., Int. Ed.*, 2016, **55**, 9898–9901.
- 31 W. Chu, X. Zhang, J. Wang, S. Zhao, S. Liu and H. Yu, *Energy Storage Mater.*, 2019, **22**, 418–423.
- 32 Y. Guo, Z. Hu, J. Wang, Z. Peng, J. Zhu, H. Ji and L. J. Wan, *Angew. Chem., Int. Ed.*, 2020, **56**, 22963–22967.
- 33 X. Zhang, G. Zhang, S. Wang, S. Li and S. Jiao, *J. Mater. Chem. A*, 2018, **6**, 3084–3090.
- 34 S. Wang, S. Jiao, J. Wang, H. S. Chen, D. Tian, H. Lei and D. N. Fang, *ACS Nano*, 2016, **11**, 469–477.
- 35 H. Jiao, D. Tian, S. Li and C. Fu, *ACS Appl. Energy Mater.*, 2018, **1**, 4924–4930.
- 36 X. Zhang, S. Jiao, J. Tu, W. L. Song, X. Xiao, S. Li, M. Wang, H. Lei, D. Tian, H. Chen and D. Fang, *Energy Environ. Sci.*, 2019, **12**, 1918–1927.
- 37 P. Nova and O. Inganos, *J. Electrochem. Soc.*, 1988, **135**, 2485–2490.
- 38 G. Li, M. Kou, J. Tu, Y. Luo, M. Wang and S. Jiao, *Chem. Eng. J.*, 2021, **421**, 127792.
- 39 X. Wang, H. Hao, J. Liu, T. Huang and A. Yu, *Electrochim. Acta*, 2011, **56**, 4065–4069.

